Chemical Engineering Journal 473 (2023) 145021

Contents lists available at ScienceDirect

Chemical Engineering Journal

journal homepage: www.elsevier.com/locate/cej

Robust Pd/Al_2O_3 bifunctional catalyst for single reactor tandem synthesis of furan and tetrahydrofuran derivatives from furfural

L. Gao [a,1], Z. Jiang [b,1], I. Miletto [c], E. Gianotti [d], E. Rebmann [b], L. Baussaron [b], F. Jiang [a], M. Pera-Titus [a,e,*]

[a] Eco-Efficient Products and Processes Laboratory (E2P2L), UMI 3464 CNRS-Solvay, 3966 Jin Du Road, Xin Zhuang Ind. Zone, 201108 Shanghai, China
[b] Solvay – Process Innovation Department, Research & Innovation Centre of Lyon, 85 Avenue des Frères Perret, 69192 Saint Fons, France
[c] Department of Pharmaceutical Sciences, Università del Piemonte Orientale, Largo Donegani 2, I-28100 Novara, Italy
[d] Department for Sustainable Development and Ecological Transition, Università del Piemonte Orientale, Piazza Sant'Eusebio 5, 13100, Vercelli, Italy
[e] Cardiff Catalysis Institute, School of Chemistry, Cardiff University, Main Building, Park Place, Cardiff CF10 3AT, UK

ARTICLE INFO

Keywords:
Furfural
Methyl isobutyl ketone
Acid catalyst
Alumina
Single-reactor

ABSTRACT

In this study, we report a reusable catalytic system based on a bifunctional Pd/Al_2O_3 spheres to conduct the single-reactor tandem aldol condensation/crotonization reaction between furfural and methylisobutyl ketone, followed by hydrogenation, both in batch and continuous mode. In batch mode, the process achieved an overall 86 % yield of 1-(tetrahydrofuran-2-yl)-5-methylhexan-3-one at 180 °C after 9 h at ~~(~~5.2 wt% furfural concentration~~)~~. The reaction rate for the aldol condensation/crotonization step decreased at higher FF concentration, suggesting the inhibition of Lewis acid centers due to adsorbed FF as inferred from kinetic modeling. In continuous mode, the catalyst was operated in a dual-type fixed bed reactor and reached 55 % steady-state conversion and 60 % and 35 % selectivity to 1-(furan-2-yl)-5-methylhexan-3-one and (E)-1-(furan-2-yl)-5-methylhex-1-en-3-one, respectively, after 12 h operation at 170 °C and a weight-hourly space velocity of 0.50 h^{-1} at high furfural concentration (18 wt%). NH_3/CO_2 temperature-programmed desorption and FT-IR spectroscopy implemented with adsorbed pyridine, NH_3 and CO_2 were used to assess the nature, strength, density and stability of the acid and basic sites.

1. Introduction

The mitigation of fossil fuels and the environmental shortcomings derived from their use is encouraging the exploration of new energy sources for the chemical industry. At present, many research strategies focus on the use of biomass-derived feedstocks as platform chemicals for the synthesis of fuels and valuable chemicals [1–4]. Most specifically, the transformation of furanic compounds, which can be produced from the hydrolysis of carbohydrates directly issued from lignocellulose, has attracted great interest [5–7].

Biobased furfural (FF) can be used as building block to access a variety of relevant industrial products and intermediates [8–13]. Furfural can undergo typical reactions of aldehydes, such as acetalization [14,15], acylation [16], aldol condensation [17], reduction to alcohols [18], reductive amination to furfurylamine [19,20], decarbonylation [21], oxidation to maleic acid/anhydride [22,23], and Grignard reactions [24]. Besides, the furan ring can be subjected to alkylation, hydrogenation, oxidation, halogenation and nitration reactions [25–30]. However, a large number of FF transformations are possible, and indeed, the use of renewable FF to produce fine and commodity chemicals and fuels is still today an underdeveloped area [31].

The aldol condensation of FF with ketones is commonly employed in the food industry, and can be used to prepare longer-chain value-added liquid fuels starting from ketones. Aldol condensation is defined as an organic reaction in which an enolate ion (i.e. carbanion generated from α-hydrogen ketone or aldehyde) reacts with a carbonyl compound (most often acetone) to form β-hydroxy ketone or β-hydroxy aldehyde, followed by dehydration (crotonization) to give a conjugated α,β-unsaturated enone. Aldol condensation reactions are commonly catalyzed by homogeneous bases such as KOH and NaOH, which are highly active, but hardly recyclable. The reaction can be either conducted in a single phase or in biphasic system [32], enabling also one-pot processes starting from carbohydrates [33]. Recent work has

* Corresponding author at: Cardiff Catalysis Institute, School of Chemistry, Cardiff University, Main Building, Park Place, Cardiff CF10 3AT, UK.
E-mail address: peratitusm@cardiff.ac.uk (M. Pera-Titus).
[1] These authors contributed equally to the manuscript.

https://doi.org/10.1016/j.cej.2023.145021
Received 27 April 2023; Received in revised form 18 July 2023; Accepted 23 July 2023
Available online 5 August 2023

Nomenclature

A	Pre-exponential factor in Arrhenius equation (mol.g^{-1}.s^{-1})
c	Concentration (mol.m^{-3})
CB	Carbon balance (–)
CI	Confidence interval of optimized parameter (–)
cov	Diagonal elements of the variance–covariance matrix (–)
Ea	Activation energy in Arrhenius equation (J.mol^{-1})
F	Total liquid flowrate (m^3.s^{-1})
J	Jacobian matric (–)
K	Adsorption constant (m^3.mol^{-1})
$M_{MIBK-FF}$	MIBK-to-FF weight ratio (–)
n	Number of moles (mol)
N	Degrees of freedom (–)
r	Reaction rate (mol.g^{-1}.s^{-1})
SSE	Sum of squares according to Eq. (13) (–)
t	Time (s)
t	Student-t (–)
V_L	Liquid volume (m^3)
$\bar{v}$	Molar volume (m^3.mol^{-1})
W	Catalyst amount (kg)
WHSV	Weight-hourly space velocity (s^{-1})
y(ξe,f)	Output molar fraction vector measured under the input vector $\xi_{e,f}$ (–)
y(ξe,f)	Predicted output molar fraction vector (–)

Greek symbols

ν	Stoichiometric coefficient (–)
Σ_y	Variance-covariance matrix for the molar fractions (–)
ρ	Density (kg.m^{-3})
θ	Surface coverage (–)

Subscripts

FF	Furfural
MIBK	Methyl isobutyl ketone

Superscripts

0	Initial value
*	Empty active site

Acronyms

ALD-1	(E)-1-(furan-2-yl)-5-methylhex-1-en-3-one
ALD-1-OH	(E)-1-(furan-2-yl)-5-methylhex-1-hydroxy-3-one
ALD-2a,b	(E/Z)-3-(furan-2-ylmethylene)-4-methyl-pentan-2-one
ALD-3	(E)-1-(furan-2-yl)-di(5-methylhex-1-en-3-one)
BAS	Brønsted acid species
BBS	Brønsted basic species
cat	Catalyst
GC	Gas chromatography
FA	Furfuryl alcohol
F-ALD-1	Hydrogenated ALD-1 (C=C) product
FF	Furfural
FID	Flame ionization detector
FT-IR	Fourier-Transformed Infrared
HPLC	High-performance liquid chromatography
HR-TEM	High-resolution transmission electron microscopy
ICP-AES	Inductively coupled plasma atomic emission spectroscopy
LAS	Lewis acid species
LBS	Lewis basic species
LH	Langmuir Hinshelwood
MIBK	Methyl isobutyl ketone
NMR	Nuclear magnetic resonance
PXRD	Powder X-ray diffraction
TCD	Thermal conductivity detector
THF-ALD-1	Hydrogenated ALD-1 (C=C + furan ring) product
TPD	Temperature-programmed desorption
TPR	Temperature-programmed reduction

targeted the design of heterogeneous basic catalysts for the aldol condensation/crotonization of FF with acetone. The catalysts are commonly based on mixed oxides enriched with sites of medium strength (*e.g.*, Mg-Zr, Mg-La, Mg-Al) [34–39], hydrotalcites and layered double hydroxides [40–43], KF/aluminas [44,45], titania [46], ZnO (in the presence of water) [47] and zeolites/zeotypes [34,48–51]. Solid acid catalysts also exhibit activity for aldol condensation reactions, even if they have been less explored. Key examples comprise Brønsted solid acids relying on zeolites with microporous [52–54] or hierarchical architectures [55,56], as well as Lewis solid acid catalysts based on Nb_2O_5 or Nb_2O_5 encapsulated in MFI zeolites [57,58], Sn/BEA [59] and Zr-MOF-808/silica hybrids [60]. This study unveils the catalytic properties and robustness of γ-alumina as Lewis solid acid catalyst for the aldol condensation/crotonization reaction of FF with methyl isobutyl ketone (MIBK).

As key innovation, the aldol condensation reaction of FF with a ketone combined with a sequential reaction has been proposed for engineering tandem reactions in a single reactor. Compared to a two-reactor process, a single-reactor tandem process affords a higher degree of intensification and avoids separation of the aldol intermediate. To this aim, combinations of catalysts or multifunctional catalysts with different active centers are required. For instance, the one-pot synthesis of biofuels and monomer precursors has been reported by combining a first aldol condensation step of FF with acetone, methyl isobutyl ketone (MIBK) or cyclopentanone, followed by hydrodeoxygenation/hydrogenation catalyzed by Pd or Pt supported over acid/base supports [61–68], Pd supported over hierarchical zeolites and propylamine-grafted mesoporous silicas [69,70] and Pt encapsulated in acid zeolites [71,72]. One-pot/single-reactor reactions have also been reported for preparing furan- and THF-derived amines by the aldol condensation reaction of FF with ketones, followed by reductive amination with NH_3 and H_2, over combined Amberlyst-26 and Ru/C or Pd/Al_2O_3 catalysts [73,74]. Key to these developments is the compatibility of the different active centers, which can show antagonistic behavior in the different steps. Moreover, the catalysts should be stable against formation of oligomers from furfural, especially in the presence of polar solvents.

Herein we report a robust catalytic system based on a bifunctional Pd/Al_2O_3 catalyst for conducting the single-reactor tandem solvent-free aldol condensation/hydrogenation reactions of FF and MIBK to access a renewable biosolvent and biofuel precursor in the branched alkane range at high yield. The process comprises two steps (Scheme 1): (1) aldol condensation/crotonization, and (2) selective hydrogenation of the aldol condensation adduct(s). The activity and robustness of the catalyst was investigated in batch and continuous dual fixed-bed reactors to devise conditions for upscaling, especially at high furfural concentration. The catalytic conditions were optimized to achieve high conversion and selectivity, as well as a high level of reusability. The nature, strength and density of acid and basic on alumina were characterized by combining NH_3/CO_2-TPD and FT-IR spectroscopy using pyridine, NH_3 and CO_2 as acid/base probe molecules. The structural properties of the catalysts and location of Pd nanoparticles on alumina were investigated using X-ray diffraction (XRD) and HR-TEM. Kinetic modeling of FF-MIBK aldol condensation over alumina in an autoclave batch reactor was carried out using a Langmuir-Hinshelwood surface reaction mechanism.

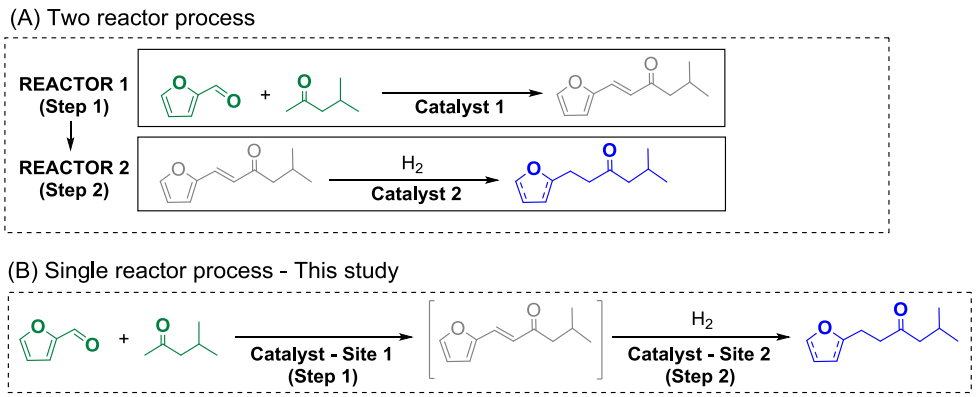

Scheme 1. Two-reactor *vs.* single reactor tandem process for the synthesis of hydrogenated derivatives from FF.

2. Materials and methods

2.1. Materials

Palladium(II) acetate (98 %), supplied by Sigma-Aldrich, was used for the synthesis of Pd/Al_2O_3 catalysts·NH_3 (≥99.7 %), purchased from SIAD (Bergamo, Italy) and 2,6-di-*tert*-butylpyridine (≥97 %), purchased from Sigma Aldrich (Milano, Italy), were used in FTIR experiments. Furfural (97 %) and methyl isobutyl ketone (≥98–100 %), used for the catalytic tests, were supplied by Sigma-Aldrich and Sinopharm/VWR Chemicals, respectively. Toluene (99.8 %) and dodecane (≥99 %) were procured from Sigma-Aldrich and used as solvent and internal standard, respectively. Gamma-alumina (Puralox SCCa-5/170, Puralox SCFa140, Puralox SBa90, alumina spheres 1.8/210, Siral 30, Siral 5 HPV) were supplied by Sasol, whereas commercial Pd/Al_2O_3, Pt/Al_2O_3, Rh/Al_2O_3 and Ru/Al_2O_3 were purchased from Johnson Matthey. Silicon carbide (120 μm) was procured from Alfa Aesar. All the chemicals, except furfural, were used as received without further purification. Furfural was distilled at 80 °C and 25 mbar using a rotavapor (R-300, Buchi).

2.2. Synthesis of Pd/Al_2O_3

Pd/Al_2O_3 was prepared by wet impregnation of Al_2O_3 spheres (5.9 g) using a precursor solution of palladium acetate (0.54 g in 30 mL acetone) under sonication. After 30 min, acetone was evaporated at 40 °C, and the catalyst was dried overnight at 80 °C, calcined at 400 °C for 4 h and reduced at 200 °C for 4 h under H_2.

2.3. Catalyst characterization

Powder X-ray diffraction (PXRD) was used to characterize the phases present in the catalysts. The patterns were obtained using a *Bruker AXS D8 ADVANCE* diffractometer in reflection mode with Bragg-Brentano geometry, operating with a radiation source of monochromatic X-rays Cu Kα (λ = 1.5406 Å) and LYNXEYE_XE_T, and applying the following acquisition parameters: voltage and amperage of the source 40 kV/40 mA; interval 5–60° (2θ).

Transmission electron microscopy (TEM) was conducted on a JEOL 2100 instrument with a LaB6 filament, an acceleration voltage of 200 kV and using a Gatan 832 CCD camera. Prior to characterization, the samples were dispersed in ethanol with ultrasonic treatment for 5 min and dropped onto a carbon film on a copper grid. The size distribution of Pd nanoparticles over Pd/Al_2O_3 was obtained by manual analysis of micrographs with Image J software.

FTIR spectra of catalyst pellets, previously outgassed at 150 °C to remove adsorbed moisture, were measured under vacuum ($<10^{-5}$ mbar) on a Bruker Equinox 55 spectrometer equipped with a pyroelectric detector (DTGS type, 4 cm^{-1} resolution). NH_3, pyridine and CO_2 were adsorbed at room temperature using a specially designed cell and evacuated using a vacuum line to carry out the adsorption–desorption *in situ* measurements. FTIR spectra were normalized by the pellet weight and plotted in differencemode. The total number of accessible Lewis and Brønsted acid sites (N) was measured using the Lambert-Beer law (A = εNρ), where A is the area of a given band (cm^{-1}), ε is the molar extinction coefficient (cm μmol^{-1}), N is the concentration of the vibrating species (μmol g^{-1}), and ρ is the density of the pellet (mg cm^{-2}) [75].

The density and strength of acid sites in the catalysts was measured by NH_3-TPD using a Micromeritics AutoChem II 2920 system equipped with a quartz U-type tubular reactor and a thermal conductivity (TCD) detector. In a typical test, the catalyst (70 mg) pre-grinded at 200 μm was pre-treated at 250 °C for 2 h under a He flow [40 mL(STP) min^{-1}] and cooled down to room temperature. Then, NH_3 was chemisorbed at 100 °C using pulsed injections, and the temperature was increased up to 1000 °C using a ramp of 10 °C min^{-1}. The density of acid sites was quantified using the method reported in refs. [76,77]. The NH_3-TPD profiles were normalized by the catalyst catalyst.

The bulk Pd content of the catalysts, previously dissolved using a HNO_3/H_2SO_4/HF solution, was measured by Inductively Coupled Plasma Atomic Emission Spectroscopy (ICP-AES) using a Thermo IRIS Intrepid II XSP atomic emission spectrometer.

2.4. Catalytic tests

The catalytic tests for the tandem aldol condensation/crotonization + hydrogenation reaction were conducted both in batch mode (autoclave reactor) and in continuous flow (dual-type fixed-bed reactor). The experimental details for the different tests are compiled in Sections 2.5.1 and 2.5.2.

Preliminary tests were carried in both operation modes to exclude a role of mass transfer effects in the catalytic activity. In the tests in autoclave, the FF conversion kept unchanged with the stirring rate in the range 500–1500 rpm. Also, dedicated tests in the fixed bed were carried out at constant weight-hourly-space-velocity (WHSV) (see definition in Section 2.5.2) of 0.25 h^{-1}, but varying the FF liquid flowrate and catalyst loading in the reactor. The application of the Mears criterion also confirmed the absence of of mass transfer resistances in the reactors (see SI).

2.4.1. Catalytic tests in batch mode

The catalytic tests were carried out primarily in a stainless steel autoclave reactor (30 mL, Taiatsu). In a given test in batch mode, 0.2 g (2 mmol) of distilled FF and 3.8 g (38 mmol) of MIBK were reacted over 40 mg of calcined catalyst [MIBK/FF 19.0 = (w/w); FF/cat = 5.0 (w/w)] in the temperature range of 120–180 °C under magnetic stirring (1000 rpm).

The same autoclave reactor was used to perform the single reactor condensation/crotonization reaction of FF and MIBK at the

experimental conditions described above for a given time, followed by hydrogenation using molecular H_2 at 80–160 °C, 10–20 bar and 6–12 h ensuring complete reduction of Pd according to the H_2-TPR profiles of the catalysts (not shown).

Additional catalytic tests for aldol condensation/crotonization reaction were conducted in a Top Industrie reactor with mechanical stirring (500–1500 rpm). In these tests, the reactor was charged with 2 g (20 mmol) of distilled FF, 38 g (380 mmol) of MIBK and 400 mg of catalyst [MIBK/FF 19.0 = (w/w); FF/cat = 5.0 (w/w)], and the reaction was carried out at 120 °C. The results in the three reactors were comparable and fully reproducible using Siral HPV as catalyst (Figure S1).

The FF conversion, selectivity, yield, initial reaction rate of formation ($r_{i,0}$) of each product and carbon balance (CB), were defined using the expressions (Eqs. (1)–(5))

$$FF\ conversion = 1 - \frac{n_{FF}}{n_{FF}^0} \times 100 \quad (1)$$

$$Selectivity_i = \frac{n_i}{n_{FF}^0 - n_{FF}} \times 100 \quad (2)$$

$$Yield_i = \frac{n_i}{n_{FF}^0} \times 100 \quad (3)$$

$$r_{i,0} = \frac{1}{W}\frac{dn_i}{dt}\bigg|_{t=0} \quad (4)$$

$$CB_{FF} = \frac{\Sigma n_i + n_{FF}}{n_{FF}^0} \times 100 \quad (5)$$

where n_i is the number of moles of product *i*, and W is the catalyst loading.

2.4.1.1. Catalytic tests in continuous flow. The catalytic tests in continuous flow were conducted in a stainless steel downflow fixed-bed reactor (i.d 19 mm, length 250 mm) (Figure S2). The reactor consisted of three layers: (bottom) 200-μm SiC to ensure the positioning of the catalyst(s) within the isothermal zone of the bed; (2) catalyst; and (3) 200-μm SiC to facilitate the feed mixing and heating to the reaction temperature.

The temperature was controlled along the bed length using a heat controller box (Top Industrie, ±1 % accuracy). The gas (H_2) and liquid were simultaneously co-added at the reactor inlet using a thermal mass flow controller (Bronkhorst, ±1 % accuracy) and a HPLC pump (PU-4086, JASCO) (±5 % accuracy), respectively. The gas–liquid mixture was depressurized along the reactor using a pressure regulator. The reactor outlet was cooled down to room temperature while passing the sampling pipe, enveloped with a cooling jacket, connected to the thermostated cooling batch (LAUDA), and liquid samples were recovered at regular times.

Two bed configurations were used for the catalytic tests: (1) a single bed of Al_2O_3 (11.5 g) to study the catalytic activity in the aldol condensation/crotonization reaction at 80 °C for 12 h using 4.8 wt% of FF (2:1 MIBK/FF molar ratio), and (2) an Al_2O_3-PdO/Al_2O_3 (11.5 g Al_2O_3 + 11.6 g PdO/Al_2O_3) dual fixed-bed reactor, where PdO/Al_2O_3 bed was placed at the bottom of the Al_2O_3 bed, and the reaction was carried out at the same conditions as in (1).

The weight-hourly space velocity of the reactor referred to FF ($WHSV_{FF}$) was computed as follows

$$WHSV_{FF}\left(h^{-1}\right) = \frac{F_T^0\,(mL/h)}{W(g)}\ \rho_T\,(g/mL)\ \frac{1}{1 + M_{MIBK-FF}\,(g/g)} \quad (6)$$

where F_T^0 is the total liquid flowrate at the reactor inlet (range 0.6–3.0 $mL.h^{-1}$), W is the catalyst loading (11.5 g), ρ_T is the total density of the liquid (0.86 g/mL) and $M_{MIBK\text{-}FF}$ is the MIBK/FF weight ratio (4.5).

The FF conversion, selectivity and yield of each product, as well as the carbon balance (CB), at the outlet of the reactor were defined using the following expressions (Eqs. (7)–(10))

$$FF\ conversion = 1 - \frac{F_{FF}}{F_{FF}^0} \times 100 \quad (7)$$

$$Selectivity_i = \frac{F_i}{F_{FF}^0 - F_{FF}} \times 100 \quad (8)$$

$$Yield_i = \frac{F_i}{F_{FF}^0} \times 100 \quad (9)$$

$$CB_{FF} = \frac{\Sigma F_i + F_{FF}}{F_{FF}^0} \times 100 \quad (10)$$

where F_{FF}^0 and F_{FF} refer to the initial and final FF molar flow, respectively, and F_i is the molar flow of product *i*.

2.5. Analysis of the reaction media

The concentration of non-reacted FF and MIBK and the reaction products were analyzed and quantified by gas chromatography on a Thermo Scientific Trace 1100 GC equipped with a flame ionization detector (FID) and a HP-5 capillary column with 5 wt% phenyl groups (length 30 m; inner diameter 0.25 mm) for the catalytic tests in autoclave, and on an Agilent GC equipped with a FID detector and a DB-5 column (30 m × 320 μm × 0.25 μm) for the catalytic tests in fixed bed. The injector and detector temperatures were set at 250 °C/300 °C and 300 °C/275 °C for the first and second GC, respectively, while the sample volume was 2 μL. In both cases, the calibration was performed using biphenyl and dodecane as internal standard for the aldolization and hydrogenation products, respectively.

^{1}H NMR analysis was used to identify the structure of organic compounds. The NMR spectra were recorded on a 400 MHz Bruker spectrometer using $CDCl_3$ as deuterated solvent. FF was identified using the aldehyde signal –C*H*O at 9.7 ppm, while the aldol condensation product (ALD-1) was characterized by the –C*H*– signal at 6.6 ppm belonging to the furan ring.

3. Theory

3.1. Kinetic modeling

A kinetic model based on a Langmuir-Hinshelwood type catalytic mechanism was developed and contrasted to rationalize the influence of the operation variables on the catalytic performance for the aldol condensation/crotonization of FF with MIBK. The model was further implemented in the reactor mass balances and integrated over the reactor volume. The mass and volume balances in an isothermal batch reactor can be expressed as follows

$$\frac{dc_i}{dt} = -\frac{c_i}{V_L}\frac{dV_L}{dt} + \sum_j^{n_r} \nu_{i,j} r_j \quad (11)$$

$$\frac{1}{V_L}\frac{dV_L}{dt} = \sum_i^{n_s} \bar{v}_i \left(\sum_j^{n_r} \nu_{i,j} r_j \right) \quad (12)$$

where c_i is the concentration of species i (i.e. FF, MIBK, ALD-1-OH, ALD-1), V_L is the liquid volume, n_s and n_r are the number of species and chemical reactions ($n_s = 4$, $n_r = 1$), respectively, $\nu_{i,j}$ is the stoichiometric coefficient of species i for reaction j, r_j is the reaction rate of the chemical reaction j, and $\bar{v}_i$ is the molar volume of species i.

3.2. Numerical approach and fittings

The kinetic model was incorporated into the mass balances (Eqs (11) and (12), resulting in a system of coupled ordinary differential equations

(ODEs). The ODEs were solved using the Matlab® functions *ode15s* with a relative tolerance of 0.1 % for the local discretization errors. The model parameters were fitted using a non-linear least-square method using a hybrid optimization algorithm combining global optimization with a genetic algorithm (ga) and local search with an interior-point algorithm (fmincon), by comparison of the experimental and predicted concentrations of FF, MIBK, ALD-1-OH, and ALD-1. Herein, the average weighted least square criterion, expressed by Eq. (13), was used for parameter estimation

$$SSE = \frac{1}{\sum_{e=1}^{n_{exp}} n_{sp_e}} \sum_{e=1}^{n_{exp}} \sum_{f=1}^{n_{sp_e}} \left[\mathbf{y}\left(\xi_{e,f}\right) - \hat{\mathbf{y}}\left(\xi_{e,f}, \theta\right)\right]^T \Sigma_y^{-1} \left[\mathbf{y}\left(\xi_{e,f}\right) - \hat{\mathbf{y}}\left(\xi_{e,f}, \theta\right)\right] \quad (13)$$

where n_{exp} is the number of experiments, n_{spe} is the number of samples in the e^{th} experiment, $\mathbf{y}\left(\xi_{e,f}\right)$ is the output molar fraction vector measured under the input vector $\xi_{e,f}$, which corresponds to the f^{th} system input vector of the e^{th} experiment, $\hat{\mathbf{y}}\left(\xi_{e,f}, \theta\right)$ is the predicted output molar fraction vector, and Σ_y is the variance–covariance matrix for the molar fractions.

In a subsequent step, the random distribution of the error, as well as the confidence interval, the degree of correlation and physical consistency of the fitted parameters, were used as descriptors to assess the quality of the kinetic model. The 95 % confidence interval for the optimized parameters (CI_j) was calculated using Eq. (14)

$$CI_j = \pm t_{1-0.05/2} \sqrt{cov_{jj}} = 1.96 \sqrt{cov_{jj}} \quad (14)$$

where $t_{1\text{-}0.05/2}$ refers to the Student-t (1.96 for 95 % confidence interval), and cov_{jj} are the diagonal elements of the variance–covariance matrix (Eq (15))

$$cov = \frac{SSE}{N_Y - N_p} \left(J^T \times J\right)^{-1} \quad (15)$$

where J is the Jacobian matrix and $(N_y - N_p)$ is the number of degrees of freedom, N_y and N_p referring to the number of experiments and parameters, respectively.

4. Results and discussion

4.1. Aldol condensation/crotonization of FF with MIBK over alumina catalysts

4.1.1. Catalyst screening in batch reactor

First, we screened the catalytic performance of a series of silica-aluminas and aluminas in batch reactor for the aldol condensation/crotonization reaction of FF and MIBK (Table 1). All the catalysts exhibit high selectivity to (E)-1-(furan-2-yl)-5-methylhex-1-en-3-one (ALD-1) (Scheme 2) with a yield up to 89 % for alumina spheres at 180 °C after 3 h (entries 1–8). The calcination temperature does not affect the selectivity of alumina in the range 100–800 °C (entries 5–7). However, the FF conversion declines slightly at the highest calcination temperature (800 °C). In all cases, the intermediate (E)-1-(furan-2-yl)-5-methylhex-1-hydroxy-3-one (ALD-1-OH) is observed, but with low selectivity (3–5 %). The high performance of alumina catalysts opposes that observed on ZnO, Al-SBA-15 (Si/Al = 76) and hierarchical HPSAPO-5 with only Brønsted acid centers (entries 9–11), where (E)- and (Z)-3-(furan-2-ylmethylene)-4-methyl-pentan-2-one (ALD-2a and ALD-2b, respectively) are also formed as by-products with a selectivity < 15 %. This contrasting behavior suggests a key role of Lewis acidity in alumina on the selectivity towards ALD-1. Besides, in all cases, no by-products issued from the aldol self-condensation/crotonization of MIBK are observed, as well as by-products from Michael addition of ALD-1 with MIBK (ALD-3).

Overall, given its high selectivity and activity towards ALD-1, Al_2O_3 was chosen as catalyst, calcined at 400 °C, for further optimization of the reaction conditions and rationalization of the reaction mechanisms. The results are presented in sections 4.1.2-4.1.4.

4.1.2. Kinetic profiles for FF + MIBK aldolization/crotonization over Al_2O_3

The kinetic profiles were measured on the Al_2O_3 spheres in batch reactor in the temperature range 120–180 °C. The initial MIBK/FF and FF/cat weight ratios were set to 19 (5.2 wt% FF) and 5.0, respectively. The FF conversion increases monotonously along the reaction, reaching almost full conversion at 180 °C after 6 h (Fig. 1). The ALD-1 selectivity is promoted by the temperature at short reaction times (<3h) until a plateau value higher than 95 %. Noteworthy, opposing a previous study [69], the by-product ALD-2a,b is not observed along the reaction. However, the alcohol intermediate (ALD-1-OH), issued from the aldol condensation reaction, is observed at low yield (<5 %). Irrespective of the temperature, the carbon balance is excellent with a value higher than 95 % at full FF conversion (Figure S3).

We measured additional kinetic profiles at variable MIBK/FF and FF/cat ratios (Figure S4) and plotted the selectivity-conversion curves (Fig. 2). Regardless of the reaction conditions, the ALD-1 selectivity displays a plateau (>90 %) at a FF conversion higher than 20 %. The ALD-1-OH selectivity reaches 50 % at only 5 % FF conversion, but decreases sharply to 10 % while increasing the FF conversion to 20 %. At higher conversion, the ALD-1-OH selectivity declines monotonously until 5 % at full conversion. No ALD-2a,b is observed irrespective of the conversion.

Overall, this body of results points out that Al_2O_3 (spheres) is an active and selective catalyst for preparing ALD-1 by the aldol

Table 1
Summary of catalytic properties for silica-aluminas and aluminas tested in this study[a].

Entry	Catalyst	Conv FF (%)	Selectivity (%)			Yield ALD-1 (%)	CB_{FF} (%)
			ALD-1-OH	ALD-1	ALD-2a,b		
1	SiO_2-Al_2O_3 (Siral 5 HPV)	75	3	97	–	73	98
2	SiO_2-Al_2O_3 (Siral 30)	67	5	89	–	60	93
3	Al_2O_3 (SCCa-5/170)	65	2	98	–	62	99
4	Al_2O_3 (SBa90)	42	4	96	–	40	98
5	Al_2O_3 (SCFa140)[b]	62	4	96	–	60	99
6	Al_2O_3 (SCFa140)	72	5	95	–	68	99
7	Al_2O_3 (SCFa140)[c]	48	5	94	–	45	94
8	Al_2O_3 spheres 1.8/210	92	3	97	–	89	100
9	ZnO [69]	25	–	76	14	19	87
10	Al-SBA-15 (Si/Al = 76) [69]	38	–	45	7	17	84
11	H-SAPO-5 [69]	73	–	62	14	46	76

[a] Reaction conditions: MIBK/FF = 19.0 (w/w), FF/cat = 5.0 (w/w), 180 °C, 3 h, catalyst calcined at 400 °C.
[b] Catalyst calcined at 100 °C.
[c] Catalyst calcined at 800 °C.

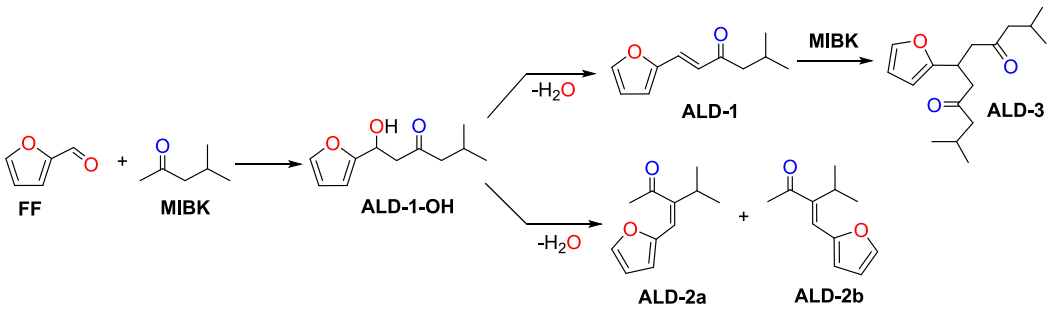

Scheme 2. Possible products obtained in the aldol condensation/crotonization reaction of FF with MIBK over alumina and silica-alumina catalysts.

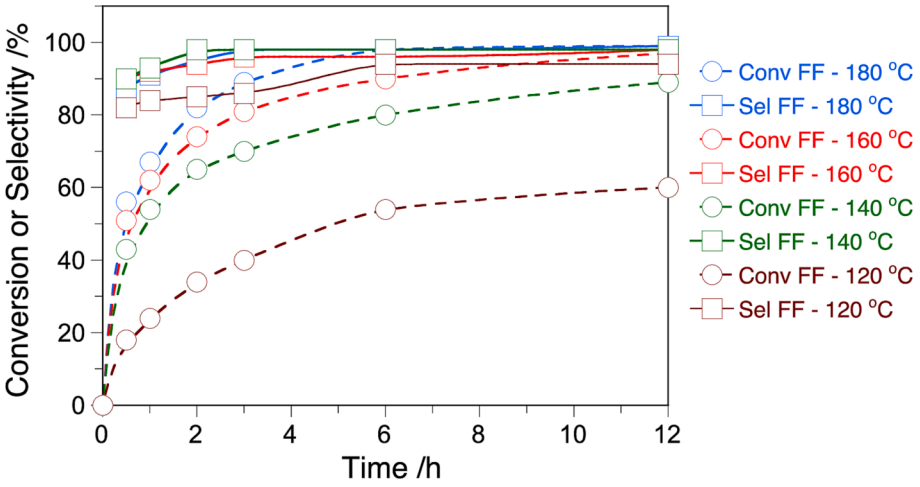

Fig. 1. Time-evolution of the FF conversion (dashed curves) and ALD-1 selectivity (straight curves) at variable temperatures in the aldol condensation/crotonization reaction of FF with MIBK over Al_2O_3 spheres. Reaction conditions: MIBK/FF ratio = 19.0 (w/w); FF/cat ratio = 5.0 (w/w), catalyst calcined at 400 °C for 2 h. The curves are a guide to the eye.

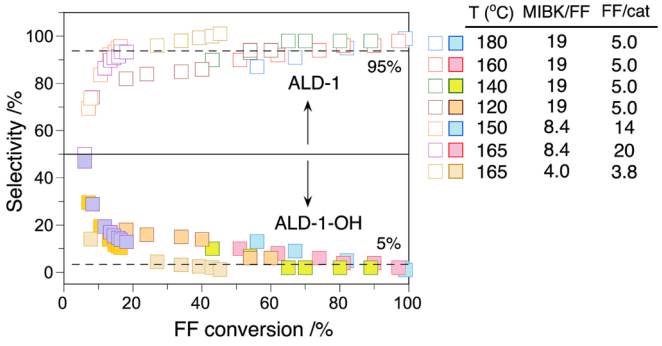

Fig. 2. Selectivity-conversion plots in the aldol condensation/crotonization reaction of FF with MIBK over Al_2O_3 spheres. Reaction conditions: T = 120–180 °C; MIBK/FF ratio = 4.0–19.0 (w/w); FF/cat ratio = 4.0–20.0 (w/w). The kinetic plots can be found in the SI (Figure S4).

condensation/crotonization reaction of FF with MIBK. The main by-product is ALD-1-OH, but its yield is lower than 5 % at high FF conversion.

4.1.3. Reaction rates and activation energies for ALD-1 synthesis

The initial reaction rates of ALD-1 formation over Al_2O_3 spheres were measured from the kinetic plots of the ALD-1 yield in batch reactor using Eq (4) and rational polynomial functions for fitting the kinetic curves (Figure S4). The highest rate (110 mmol.g^{-1}.h^{-1}) is obtained at 180 °C for a MIBK/FF ratio of 19.0 (w/w), which is comparable to the rate measured on hierarchical SAPO-5 [69]. The reaction rate increases with the MIBK/FF ratio (i.e. lower FF concentration) (Figure S5), suggesting a possible inhibition of the active centers by adsorbed FF. We measured the apparent activation energy for ALD-1 formation by representing the Arrhenius plots (see also Figure S5). The apparent activation energy is about 38 kJ/mol, which is much lower than the value measured on microporous and hierarchical SAPO-5 catalysts (~100 kJ/mol) [69]. This observation combined with the much higher ALD-1 selectivity suggests a facilitated activation of the aldol condensation/crotonization reaction of FF with MIBK on Lewis acid centers compared to Brønsted acid centers when comparing the catalytic results over Al_2O_3 and SAPO-5.

4.1.4. Catalytic mechanism for ALD-1 synthesis over alumina spheres

The high activity and selectivity of Al_2O_3 spheres for the aldol condensation/crotonization reaction of FF with MIBK prompted us to study in more detail the catalytic mechanism. To this aim, we developed a Langmuir-Hinshelwood (LH) kinetic model to rationalize the experimental trends, with emphasis on the inhibition effect of FF on the reaction rate. In line with the experimental observations, the following assumptions were considered:

1. The FF-MIBK system was represented by two main reactions, i.e. aldol condensation of FF with MIBK to ALD-1-OH, and crotonization reaction of ALD-1-OH to ALD-1;
2. Langmuir-Hinshelwood (LH) surface reaction mechanisms were considered involving the surface reaction between adsorbed MIBK and FF;
3. The surface reaction was considered as rate limiting;
4. Langmuir-type FF and MIBK adsorption models were taken into account.

Table 2
Elementary steps for the best model and rate equations (* = empty active site).

Step	Elementary reaction	Rate equation
1	$FF + * \Leftrightarrow^{K_{FF}} FF*$	$K_1 = \frac{\theta_{FF*}}{c_{FF}\,\theta^*}$
2	$MIBK + * \Leftrightarrow^{K_{MIBK}} MIBK*$	$K_2 = \frac{\theta_{MIBK*}}{c_{MIBK}\,\theta^*}$
3	$FF* + MIBK* \overset{k_1}{\rightarrow} ALD1-OH*$	$r_3 = A_3 \exp\left(-\frac{Ea_3}{RT}\right)\theta_{MIBK*}\theta_{FF*}$
4	$ALD1-OH* \overset{k_2}{\rightarrow} ALD1* + H_2O*$	$r_4 = A_4 \exp\left(-\frac{Ea_4}{RT}\right)\theta_{ALD1-OH*}$
5	$ALD1-OH + * \Leftrightarrow^{K_{ALD1-OH}} ALD1-OH*$	$K_5 = \frac{\theta_{ALD1-OH*}}{c_{ALD1-OH}\,\theta^*}$
6	$ALD1 + * \Leftrightarrow^{K_{ALD1}} ALD1*$	$K_6 = \frac{\theta_{ALD1*}}{c_{ALD1}\,\theta^*}$
7	$H_2O + * \Leftrightarrow^{K_{H_2O}} H_2O*$	$K_7 = \frac{\theta_{H_2O*}}{c_{H_2O}\,\theta^*}$

Taking into account the above assumptions, we developed different rate equations that were fitted to the experimental data. Table 2 lists the different elementary steps with the corresponding rate equations and equilibrium expressions. In Table 2, A and E_a represent the activation energy and preexponential factors, respectively, whereas θ_i and θ^* refer to the surface coverage of species i and empty actives sites, respectively.

For a LH mechanism, the reaction rates for ALD-1-OH and ALD-1 formation can be expressed from steps 3 and 4, respectively, as follows:

$$r_3 = A_1 \exp\left(-\frac{Ea_1}{RT}\right)\theta_{MIBK*}\theta_{FF*} \quad (16)$$

$$r_4 = A_2 \exp\left(-\frac{Ea_2}{RT}\right)\theta_{ALD1-OH*} \quad (17)$$

where A and E_a are the pre-exponential factor and activation energy, respectively.

Assuming adsorption equilibrium for the different species on the catalysts surface, Eqs. (16) and (17) can be rewritten using the following expressions

$$r_3 = A_1 \exp\left(-\frac{Ea_1}{RT}\right) K_{MIBK} K_{FF} C_{MIBK} C_{FF} \theta_*^2 \quad (18)$$

$$r_4 = A_2 \exp\left(-\frac{Ea_2}{RT}\right) K_{ALD1-OH} C_{ALD1-OH} \theta_* \quad (19)$$

Table 3
Elementary steps for the best model and rate equations.

Parameter	Estimated value	CI (95%)
A_3 [$\times 10^4$ mmol·s^{-1}·g$_{cat}^{-1}$]	3.89	[3.88, 3.91]
Ea_3 [$\times 10^4$ J·mol^{-1}]	4.04	[4.04, 4.04]
A_4 [$\times 10^4$ mmol·s^{-1}·g$_{cat}^{-1}$]	5.09	[5.06, 5.11]
Ea_4 [$\times 10^4$ J·mol^{-1}]	3.49	[3.48, 3.49]
K_1 [$\times 10^{-3}$ m^3·mol^{-1}]	1.05	[1.05, 1.06]
K_2 [$\times 10^{-3}$ m^3·mol^{-1}]	5.82	[5.76, 5.89]
K_3 [$\times 10^{-3}$ m^3·mol^{-1}]	5.90	[5.87, 5.94]
K_4 [$\times 10^{-3}$ m^3·mol^{-1}]	6.82	[6.77, 6.91]
K_5 [$\times 10^{-3}$ m^3·mol^{-1}]	9.10	[4.18, 19.82]

The surface coverage of empty sites can be expressed as follows

$$\theta_* = \frac{1}{1 + K_{FF}C_{FF} + K_{MIBK}C_{MIBK} + K_{ALD1-OH}C_{ALD1-OH} + K_{ALD1}C_{ALD1} + K_{H_2O}C_{H_2O}} \quad (20)$$

The kinetic expressions for r_3 and r_4 combined with the expressions for adsorption equilibrium (steps 1, 2, 5–7) and Eq. (20) were implemented to the mass balances in Eq 11–12. The differential equations were solved numerically, and the parameters of the kinetic model (i.e. Ea_3, Ea_4, A_3, A_4, K_1, K_2, K_5, K_6, K_7) were fitted by comparison of experimental and predicted mass fractions with a correlation coefficient >0.93. Fig. 3 plots representative fittings of kinetic curves and a parity plot, whereas the parity plots for all the experiments are shown in the SI (Figure S6). The fitted parameters are listed in Table 3. The model reproduces conveniently the experimental trends and confirms the inhibiting role of FF on the reaction rate for ALD-1 formation. Also noteworthy, the activation energies for steps 3 and 4 (i.e. 40.4 kJ/mol and 34.9 kJ/mol, respectively) compare well with the apparent activation energy measured from the experimental Arrhenius plots (i.e. 38 kJ/mol, Figure S5).

4.1.5. Catalyst recyclability and reuse

We measured the recyclability and reuse of Al_2O_3 spheres in six consecutive catalytic runs for the aldol condensation/crotonization reaction at 180 °C for 3 h (Fig. 4). The 1st run results in a 90 % FF conversion and an ALD-1 selectivity of 98 %. The FF conversion declines slightly to 82 %, whereas the ALD-1 selectivity keeps unchanged. The FF conversion and ALD-1 selectivity are almost constant after the 3rd–5th runs which reveals high catalyst stability during the reaction even if some oligomers might generate. Further catalyst calcination at 400 °C

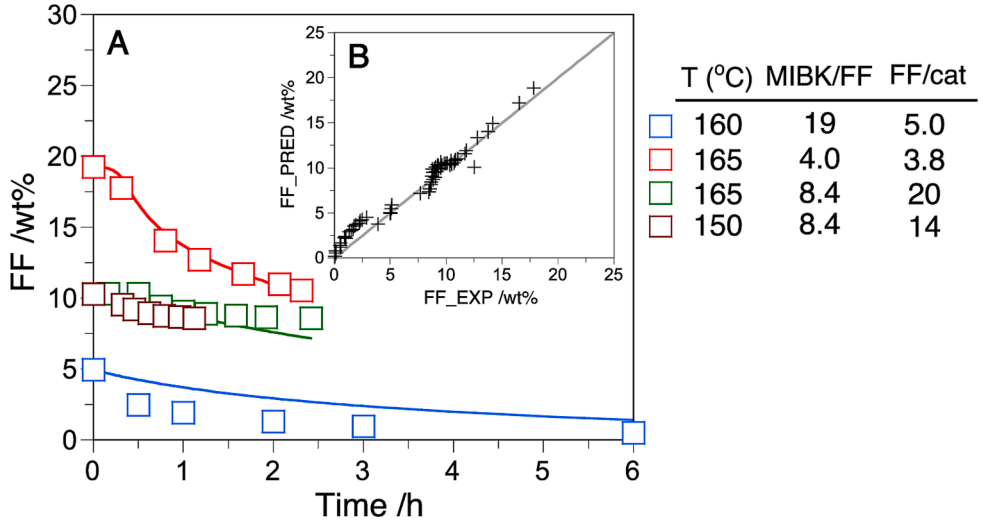

Fig. 3. (A) Experimental and fitted curves using the model depicted in Table 2; (B) parity plot. Additional parity plots can be found in Figure S6. Reaction conditions: T = 120–180 °C; MIBK/FF ratio = 4.0–19.0 (w/w); FF/cat ratio = 4.0–20.0 (w/w).

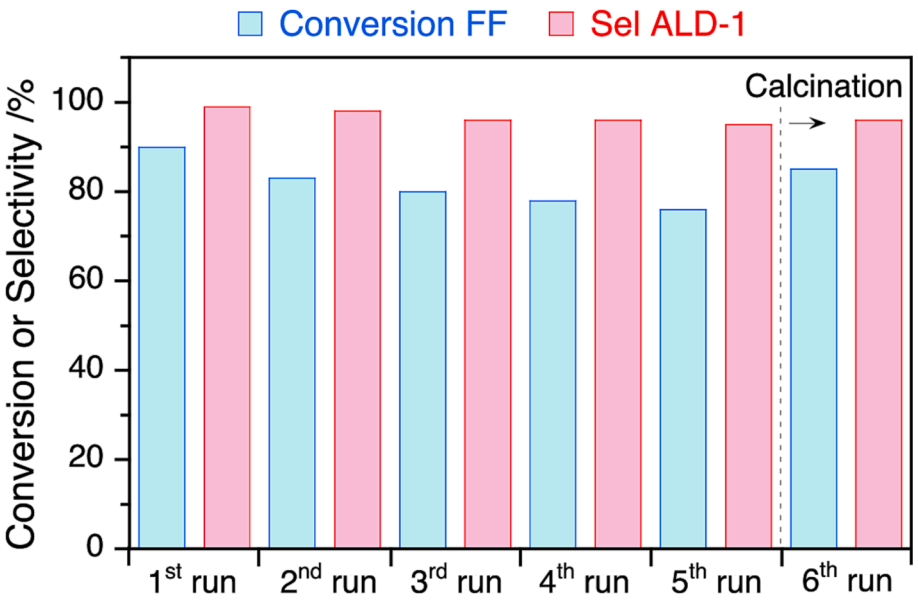

Fig. 4. Recyclability and reuse of Al_2O_3 spheres in six consecutive runs after washing with ethanol and calcination at 400 °C (6th run) under airflow. Reaction conditions: T = 180 °C, time = 3 h, MIBK/FF ratio = 19.0 (w/w); FF/cat ratio = 5.0 (w/w). The carbon balance was >95 % for all the runs.

under airflow after the 5th run resulted in a total recovery of the initial FF conversion (82 %).

4.2. Single-reactor aldol condensation/crotonization + hydrogenation reactions

Given the results in section 4.1, we designed single reactor for conducting the tandem aldol condensation/crotonization-hydrogenation reaction. We prepared three metal-supported catalysts, i.e. Pd/Al_2O_3, Pt/Al_2O_3 and Ru/Al_2O_3, at 5 wt% nominal metal loading, by impregnating the corresponding metal precursor over Al_2O_3 spheres in acetone. First, we investigated ALD-1 hydrogenation at 180 °C for 3 h and 20 bar H_2 pressure (Table 4 entries 1–3). The main hydrogenation products are F-ALD-1 issued from the hydrogenation of the conjugated C=C bond, and THF-ALD-1 issued from further hydrogenation of the furan ring. The highest selectivity is obtained over Pd/Al_2O_3 (92 %), and accordingly this catalyst was used hereinafter for engineering a single reactor process.

We then investigated the catalytic performance of unreduced PdO/Al_2O_3 catalyst in the aldol condensation/crotonization reaction of FF with MIBK at 180 °C and MIBK/FF and FF/cat ratios of 19.0 (w/w) and 5.0 (w/w), respectively (Figure S7). The kinetic profile for ALD-1 formation compares well to that measured on the parent Al_2O_3 spheres. However, ALD-3 by-product is observed with a yield lower than 10 % arising from the Michael reaction of ALD-1 with MIBK (Scheme 3, Table 4 entries 4–6).

With these results, we engineered a batchwise single-reactor tandem process over PdO/Al_2O_3 (Fig. 5, Table 4 entries 7–8). The aldol condensation/crotonization reaction was first carried out at 180 °C for 3 h, then H_2 (20 bar) was introduced to the reactor, and the hydrogenation reaction was conducted at 180 °C for 6 h. A maximum THF-ALD-1 yield of 86 % is achieved at 180 °C after 6 h, while the yield of the fully hydrogenated product of ALD-3 (i.e·THF-ALD-3) is lower than 7 %. For comparison, when the hydrogenation reaction was conducted at 180 °C for 6 h and 20 bar H_2 after the aldol condensation/crotonization reaction, the F-ALD-1 and THF-ALD-1 yields decline drastically at the expense of ALD-3, the latter reaching a maximum yield of 32 %, while the yield of THF-ALD-3 increases slightly to 12 % (Table 4, entry 9). Besides, the Interestingly, no furfuryl alcohol (FA) is observed from direct FF hydrogenation.

Overall, this body of results points out the feasibility of a batchwise single-reactor tandem process for the aldol condensation/crotonization reaction of FF with MIBK, followed by hydrogenation. In this process, THF-ALD-1 as main hydrogenation product, whereas the F-ALD-1 is only favored in a narrow window of operation between 3.5 and 4.0 h.

Table 4
Main products obtained in the single-reactor tandem aldol condensation/crotonization reaction of FF with MIBK, followed by hydrogenation.

Entry	Catalyst	Reaction conditions		Yield/%					
		1st step [a]	2nd step [b]	ALD-1-OH	ALD-1	ALD-3	F-ALD-1	THF-ALD-1	THF-ALD-3
1	Pd/Al_2O_3 [c]	–	180 °C, 3 h, 20 bar H_2	–	–	–	–	92%	–
2	Pt/Al_2O_3 [c]	–	180 °C, 3 h, 20 bar H_2	–	–	–	27 %	64 %	–
3	Ru/Al_2O_3 [c]	–	180 °C, 3 h, 20 bar H_2	–	–	–	40 %	48 %	–
4	Al_2O_3	180 °C, 3 h	–	<3 %	92 %	<1 %	–	–	–
5	PdO/Al_2O_3	180 °C, 3 h	–	<3 %	85 %	4 %	–	–	–
6	PdO/Al_2O_3	180 °C, 6 h	–	<3 %	84 %	7 %	–	–	–
7	Pd/Al_2O_3 [c]	180 °C, 3 h	180 °C, 6 h, 20 bar H_2	<3 %	–	–	–	86 %	7 %
8	PdO/Al_2O_3	180 °C, 3 h	180 °C, 6 h, 20 bar H_2	<3 %	–	–	–	87 %	6 %
9	PdO/Al_2O_3	180 °C, 6 h	100 °C, 6 h, 20 bar H_2	<3 %	32 %	–	27 %	29 %	12 %

[a] Reaction conditions: MIBK/FF = 19.0 (w/w), FF/cat = 5.0 (w/w), 180 °C, 3 h; catalysts (Al_2O_3 spheres, powder) calcined at 400 °C.
[b] Reaction conditions (entries 7–9): MIBK/ALD-1 = 19.0 (w/w), ALD-1/cat = 5.0 (w/w), 180 °C, 3 h; catalysts (Al_2O_3 spheres, powder) calcined at 400 °C.
[c] Catalyst pre-reduced at at 200 °C for 4 h under H_2 before use.

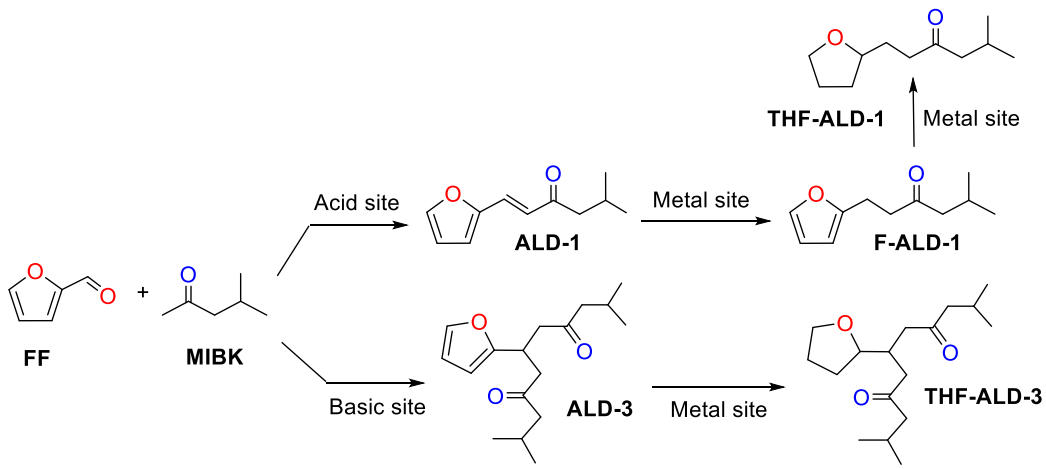

Scheme 3. Products obtained in the aldol condensation/crotonization reaction of FF with MIBK over unreduced PdO/Al_2O_3 (spheres).

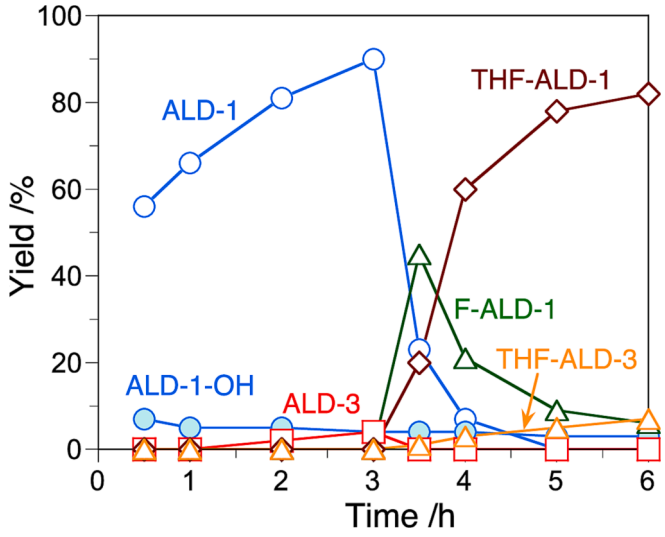

Fig. 5. Time-evolution of the ALD-1, ALD-3, F-ALD-1 and THF-ALD-1 yield in a single-reactor tandem aldol condensation/crotonization – hydrogenation process over PdO/Al_2O_3 spheres. Reaction conditions: (**step 1**) MIBK/FF ratio = 19.0 (w/w); FF/cat ratio = 5.0 (w/w), T = 180 °C, 3 h; (**step 2**) T = 180 °C, H_2 pressure = 20 bar. The catalyst was calcined at 400 °C for 2 h and reduced *in situ* during the second step. The curves are a guide to the eye.

4.3. Catalytic tests in fixed-bed reactor

We further tested the catalytic performance of Al_2O_3 and Pd/Al_2O_3 spheres in a fixed-bed reactor operated in continuous mode (see Experimental section in the SI for details) (Figure S8 and S9). The catalytic tests were conducted at a MIBK/FF weight ratio of 4.5, a temperature range of 140–200 °C and a WHSV range of 0.48–2.40 h^{-1}, under a N_2 (Al_2O_3) and H_2 (Pd/Al_2O_3) flow, respectively. Over Al_2O_3 (WHSV = 0.48 h^{-1}), the FF conversion exhibits a sustained decline during 2 h on stream at 140 °C and is enhanced at higher temperature (160 °C) until 9 h, to reach a steady state value about 20 % (without N_2) (Figure S8). In all the tests, the ALD-1 selectivity is almost 100 % with minor formation of ALD-1-OH.

Further catalytic tests were conducted over Pd/Al_2O_3 spheres to assess the formation of hydrogenated products (Figure S9). Setting the reaction conditions at 170 °C and WHSV = 1.20 h^{-1} (I), the FF conversion exhibits a monotonous decline until 25 % with preferential FA formation at 60 % selectivity. ALD-1 and ALD-1-OH are generated with <10 % selectivity, whereas THF-ALD-1 is favored compared to F-ALD-1 with 15 % selectivity. Rising the temperature to 185 °C at WHSV = 1.20 h^{-1} (II) promotes the FF conversion to 30 % while reducing the FA selectivity to 37 % in detriment of THF-ALD-1 (30 %) and ALD-1 (15 %). This trend is amplified by further increasing the temperature to 200 °C at WHSV = 1.20 h^{-1} (III) with the FA selectivity declining to 20 % and the THF-ALD-1 and ALD-1 selectivity reaching in both cases 30 %. Finally, keeping the temperature constant at 170 °C and decreasing the WHSV from 2.40 h^{-1} to 0.80 h^{-1} (IV-VI) induces a decline of the FF conversion until a steady state value of 20 % in favor of FA with a selectivity about 55 %.

To discourage FA formation, we combined Al_2O_3 and Pd/Al_2O_3 in a single-reactor dual fixed-bed reactor (see also Experimental section in the SI for details) (Fig. 6). We built a reactor including 11.5 g of Al_2O_3 and 11.6 g of Pd/Al_2O_3 (WHSV = 0.25 h^{-1}) and fed FF and MIBK at 160 °C at a flowrate of 0.6 mL/min (MIBK/FF = 4.5 w/w), and H_2 at a flowrate of 600 mL(STP)/min, respectively. The catalyst displays a stable performance during the first 7 h on stream at full FF conversion with preferential formation of ALD-1 and F-ALD-1 at 55 % and 40 % selectivity, respectively, and ALD-1-OH, THF-ALD-1 and FA with a selectivity lower than 3 %. After this period, the catalyst exhibits sustained deactivation with the FF conversion decreasing to 40 %. The ALD-1-OH selectivity keeps stable in the range 45–60 %, while the F-ALD-1

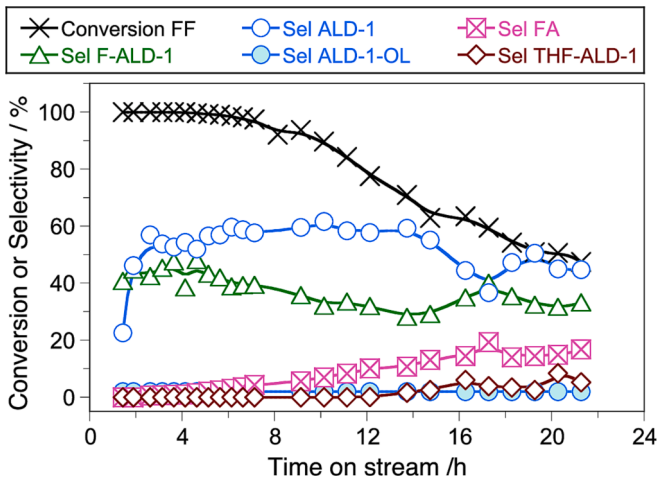

Fig. 6. Time-evolution of the FF conversion and selectivity to the different products over PdO/Al_2O_3 spheres in single-reactor dual fixed-bed reactor aldol condensation/crotonization – hydrogenation process. Reaction conditions: temperature = 170 °C; MIBK/FF ratio = 4.5 (w/w), feed flowrate = 0.6 mL/min; H_2 flowrate = 600 mL (STP)/min, pressure = 13 bar, cat = 11.5 g Al_2O_3 + 11.6 g Pd/Al_2O_3, WHSV = 0.25 h^{-1}. The catalysts were calcined at 400 °C for 2 h and PdO/Al_2O_3 was reduced *in situ* during the second step.

selectivity declines to 35 % with concomitant increase of the THF-ALD-1 selectivity to 18 %. The FA selectivity shows only a slight increase to 5 %.

Overall, compared to batch mode operation, a single-reactor dual fixed-bed reactor allows preferential formation of F-ALD-1 as main hydrogenation product together with ALD-1 unlike THF-ALD-1 with negligible FA formation.

4.4. Understanding the structure and acid properties of Pd/Al_2O_3

Given the enhanced activity and selectivity of Pd/Al_2O_3 (spheres) for the synthesis of THF-ALD-1 and F-ALD-1 in a single-reactor operated batchwise and in continuous-flow dual fixed bed mode, respectively, we explored the structural and textural properties of the bifunctional catalyst, as well as the acidity and acid strength.

4.4.1. Structural properties of Pd/Al_2O_3 and Al_2O_3

The XRD patterns of Al_2O_3 and PdO/Al_2O_3 reveal typical reflections of the Al_2O_3 phase (Figure S10). Neat reflections belonging to the PdO are visible at $2\theta = 34°$, 43° and 55°, which are indicative of the presence of Pd nanoparticles with a size>5 nm (6.3 nm estimated by Scherrer equation). This size is compatible with the average particle size measured by HR-TEM on crushed Pd/Al_2O_3 (3.3 nm). Representative HR-TEM micrographs of the crushed Pd/Al_2O_3 spheres together with the size distribution of Pd nanoparticles can be found in the SI (Figure S11).

4.4.2. Acid-base properties of crushed Al_2O_3, PdO/Al_2O_3 and Pd/Al_2O_3

It is known that Al_2O_3 have both acid and basic character. To study the acid-base properties of Al_2O_3 and the effect of the presence of PdO and Pd, FTIR spectroscopy was implemented using probe molecules with different acid-base properties after pre-treating the samples at 150 °C matching the active temperature for the aldol condensation/crotonization of FF with MIBK (120–180 °C, Fig. 1). The results and discussion are presented in the following lines.

4.4.2.1. In situ vibrational FTIR spectroscopy using basic probes (pyridine, NH_3). The FTIR spectra in the OH stretching region of the crushed Al_2O_3 and PdO/Al_2O_3 spheres after outgassing at 150 °C for 90 min, and Pd/Al_2O_3 after reduction at 150 °C under H_2 flow, reveal typical OH vibrations of the Al_2O_3 support that are not affected by the presence of PdO and Pd (Figure S12). The weak signals at 3740 and 3680 cm^{-1} can be attributed to the O–H stretching mode of terminal Al^{VI}-OH groups, where Al is in octahedral coordination, and bi-bridged (A^{IV}-OH-Al^{IV}) groups, respectively. Besides, the broad band centered at 3570 cm^{-1} can be assigned to tri-bridged (A^{IV}-O(Al^{IV})H-Al^{IV}) groups and H-bonded hydroxyl groups [78]. The latter band vanishes by treating the samples at higher temperature.

To elucidate the nature of acid sites on Al_2O_3, pyridine was used as basic probe and its adsorption at room temperature was monitored by FTIR spectroscopy. Pyridine is a well-established probe molecule for investigating and quantifying the surface acidity of solid catalysts. In particular, the vibrational ring modes in the range 1700–1400 cm^{-1} are the most sensitive with regards to the nature and strength of the adsorptive interaction [78–80]. The bands centered at 1613 (ν_{8a}), 1592 (ν_{8b}), 1492 (ν_{19a}) and 1450 (ν_{19b}) cm^{-1} correspond to pyridine coordinated to Lewis acid sites, and are present in all three samples after desorption at 150 °C (Fig. 7, curves c). The density of Lewis acid species (LAS) (N_{LAS}) were calculated by the integrated area of the 1450 cm^{-1} peak upon outgassing the catalysts at 150 °C with $\varepsilon = 2.22$ cm/µmol [81]. The density of LAS is comparable for Al_2O_3 and PdO/Al_2O_3 with a value about 94.5 µmol/g (Table 5), whereas it increases slightly for Pd/Al_2O_3 after reduction. The band ascribed to protonated pyridine is very tiny yet visible at 1545 cm^{-1} resulting in a density of Brønsted acid species (BAS) lower than 4 µmol/g for all the samples.

In a second set of experiments, NH_3 was adsorbed at room temperature and 30 mbar to qualitatively investigate the acidity of the different catalysts (reliable extinction coefficients are hardly available) (Fig. 8). NH_3 has stronger basicity than pyridine and the formation of NH_4^+

Table 5
Density of accessible acid Brønsted/Lewis acid sites (BAS/LAS) and Brønsted/Lewis basic sites (BBS/LBS) in fresh Al_2O_3, PdO/Al_2O_3 and Pd/Al_2O_3 crushed spheres.

Catalysts	Density of acid sites (µmol/g)		Density of basic sites (µmol/g)
	LAS[a]	BAS[a]	LBS/BBS[b]
Al_2O_3	93.2 (76)	3.6	195
PdO/Al_2O_3	95.9 (85)	2.4	177
Pd/Al_2O_3	101.3 (186)	3.0	–

[a] Measured from FTIR spectroscopy using pyridine as acid probe. In parentheses, data measured by NH_3-TPD (band centered at 350 °C).
[b] Measured by CO_2-TPD (band centered at 320 °C).

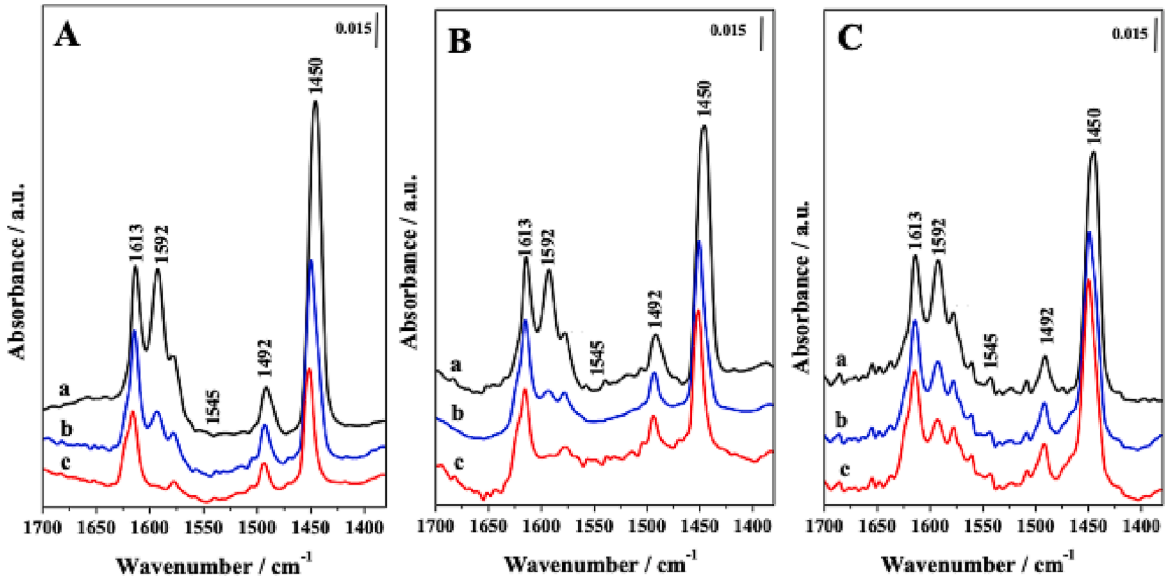

Fig. 7. FTIR difference and normalized spectra of adsorbed pyridine at room temperature on Al_2O_3 (A), PdO/Al_2O_3 (B) and Pd/Al_2O_3 (C) at various desorption temperatures: 25 °C (curves a), 100 °C (curves b) and 150 °C (curves c). The samples were outgassed at 150 °C before measuring the spectra.

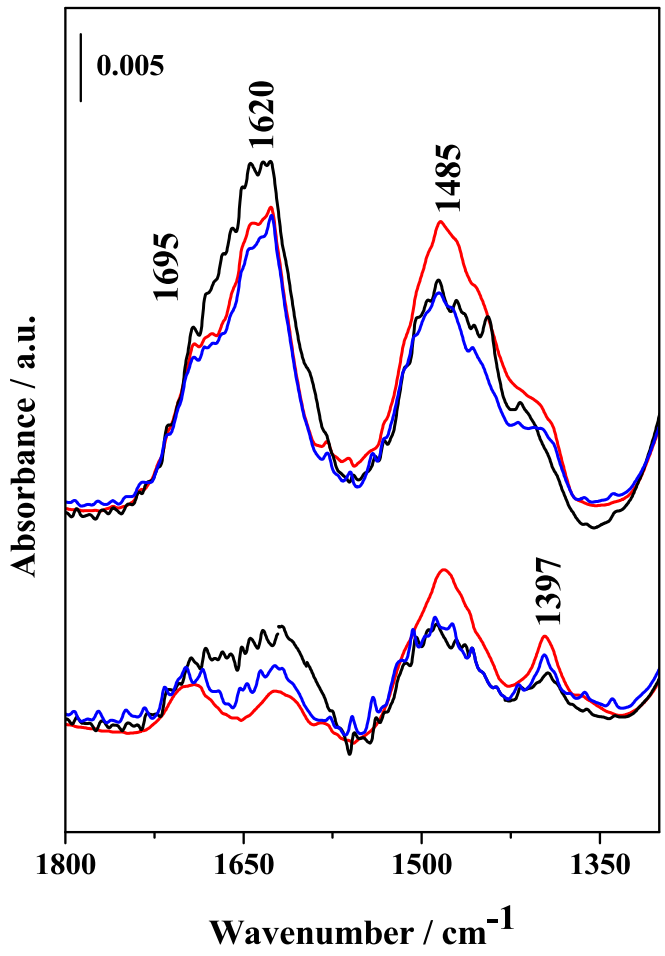

Fig. 8. FTIR difference and normalized spectra of Al_2O_3 (black curve), PdO/Al_2O_3 (red curve) and Pd/Al_2O_3 (blue curve) upon adsorption of NH_3 (30 mbar) at 25 °C (upper spectra) and upon outgassing NH_3 at 25 °C (lower spectra). The samples were outgassed at 150 °C before measuring the spectra.

species on Brønsted acid sites (bending modes centered at 1695, 1485, 1397 cm^{-1}) is clearly visible in all three catalysts after NH_3 adsorption and degassing, matching earlier observations [78,82]. This result points out that OH acid groups on the Al_2O_3 surface are strong enough to protonate NH_3, although the acid strength is expected to be weak, since they can be hardly be visualized in the FT-IR spectra using pyridine as basic probe. The band centered at 1620 cm^{-1} can be attributed to the bending mode of NH_3 adsorbed on Lewis acid sites [78]. Finally, a band is also visible at 1100 cm^{-1} upon contact of the samples with NH_3 that be attributed to physisorbed NH_3 on Al-OH groups (not shown), which vanishes after outgassing at room temperature.

4.4.2.2. In situ vibrational FTIR spectroscopy using CO_2 as acid probe. It is well known that Al_2O_3, besides its acid properties, can incorporate basic centers. To characterize the basic centers of the three samples, we monitored the FTIR spectra of the different samples after adsorbing CO_2 as acid probe molecule at room temperature and 15 mbar (Fig. 9). At room temperature, CO_2 can linearly interact with defective surface Al^{3+} cations (band at 2344 cm^{-1}) or generate bicarbonate-like species (bands at 1647 and 1435 cm^{-1} due to C-O stretching, and band at 1228 cm^{-1} due to O–H bending) [78,83,84]. The intensity of these bands is systematically lower for Pd/Al_2O_3, and in all cases decreases after outgassing the samples from 25 °C to 125 °C. In particular, the intensity of the band at 2344 cm^{-1} decreases dramatically for PdO/Al_2O_3 and Pd/Al_2O_3 compared to the parent Al_2O_3, especially for the latter sample, and the band vanishes almost completely upon heating. Noteworthy, no distinctive bands belonging to CO_2 adsorption on Pd nanoparticles are observed [85–87]. Overall, these results suggest that Pd nanoparticles might be located on basic defective sites of Al_2O_3, thus efficiently blocking them for CO_2 adsorption.

4.4.2.3. NH_3-TPD. NH_3-TPD was used to gain insight into the density distribution and strength of acid sites on Al_2O_3, PdO/Al_2O_3 and Pd/Al_2O_3 calcined at 400 °C (Fig. 10, Table S1). The NH_3-TPD profile of calcined Al_2O_3 below the calcination temperature (400 °C) (Fig. 10A, Table S1 entry 1) can be deconvoluted into four bands centered at 85, 120, 182 and 258 °C that can be attributed to weakly acid sites and NH_4^+.$n$$NH_3$ associations promoted by H-bonding, and by a further band centered at 300 °C that can be attributed to acid sites with medium strength. The sample exhibits five bands above the calcination temperature that are centered at 418, 436, 500 and 670 and 800 °C. The former three bands can be ascribed to acid sites with medium strength, whereas the latter two bands correspond to strong acid sites. By integrating the NH_3-TPD profiles, the density of the latter two bands is 79 μmol.g^{-1}, which is comparable to the density measured by FTIR spectroscopy using pyridine as molecular probe (93.2 μmol/g). Accordingly, the latter bands can be tentatively ascribed to strong Lewis acid sites, which are expected to be active for the aldol condensation/crotonization reaction of FF with MIBK.

The NH_3-TPD profile of the spent Al_2O_3 after the aldol condensation/crotonization reaction at 180 °C is similar to that of the fresh catalyst (Fig. 10B, Table S1 entry 2). However, the first two bands centered at 85 and 120 °C ascribed to weak acid sites and NH_4^+.$n$$NH_3$ associations vanish, which can be explained by partial dehydroxylation of the sample during reaction/calcination. The band belonging to medium-strength acid sites centered at 300 °C is also visible with a density about 64 μmol.g^{-1}. Above the calcination temperature, the band appearing at 418 °C shifts to 376 °C with a density about 71 μmol.g^{-1}, whereas two additional bands belonging to acid sites with intermediate acid strength are visible at 469 and 494 °C, but with a lower density (14 *vs* 30 μmol.g^{-1} and 53 *vs* 164 μmol.g^{-1}, respectively). Finally, the band originally appearing at 670 °C vanishes, whereas the band centered at 800 °C is still observed, but showing a lower acid density (7.1 μmol.g^{-1}). Overall, these observations point out that the strongest acid sites are only partially poisoned during the reaction due to water generation or furfural/ALD-1 oligomerization, promoting the catalyst stability and allowing catalysts recyclability.

The NH_3-TPD profiles were also measured on PdO/Al_2O_3 and Pd/Al_2O_3 (Fig. 10C-D, Table S1 entries 3–4). In both cases, the profiles are similar to that of fresh Al_2O_3. However, the first band centered at 85 °C vanishes, while the second band centered at 120 °C is not present for PdO/Al_2O_3 and shifts to higher temperature for Pd/Al_2O_3, suggesting partial dehydroxylation of alumina during Pd impregnation. An additional band is visible at 217 °C for PdO/Al_2O_3. In the case of PdO/Al_2O_3, the band centered at 258 °C is not visible, whereas an additional band centered at 275 °C appears for both samples that is not present in the Al_2O_3 profile. The bands belonging to acid sites with intermediate strength (i.e. 360, 452, 550 °C) are still visible after Pd impregnation with densities about 85/186 μmol.g^{-1}, 82/162 μmol.g^{-1} and 81/210 μmol.g^{-1}, respectively. The density of strong acid sites is 62 and 69 μmol.g^{-1} for PdO/Al_2O_3 and Pd/Al_2O_3, respectively, which is comparable to the value measured on Al_2O_3.

4.4.2.4. CO_2-TPD. CO_2-TPD was used to measure the density distribution and strength of basic sites (Brønsted and Lewis, BBS and LBS, respectively) on Al_2O_3 and PdO/Al_2O_3 calcined at 400 °C (Figure S13, Table S2). The CO_2-TPD profile of calcined Al_2O_3 below the calcination temperature (Fig. S13A, Table S2 entry 1) is similar to that measured by NH_3-TPD for probing the surface acidity. The profile can be deconvoluted into five bands centered at 87, 125, 166, 195 and 225 °C that can be attributed to weakly basic sites promoted by H-bonding, and by a

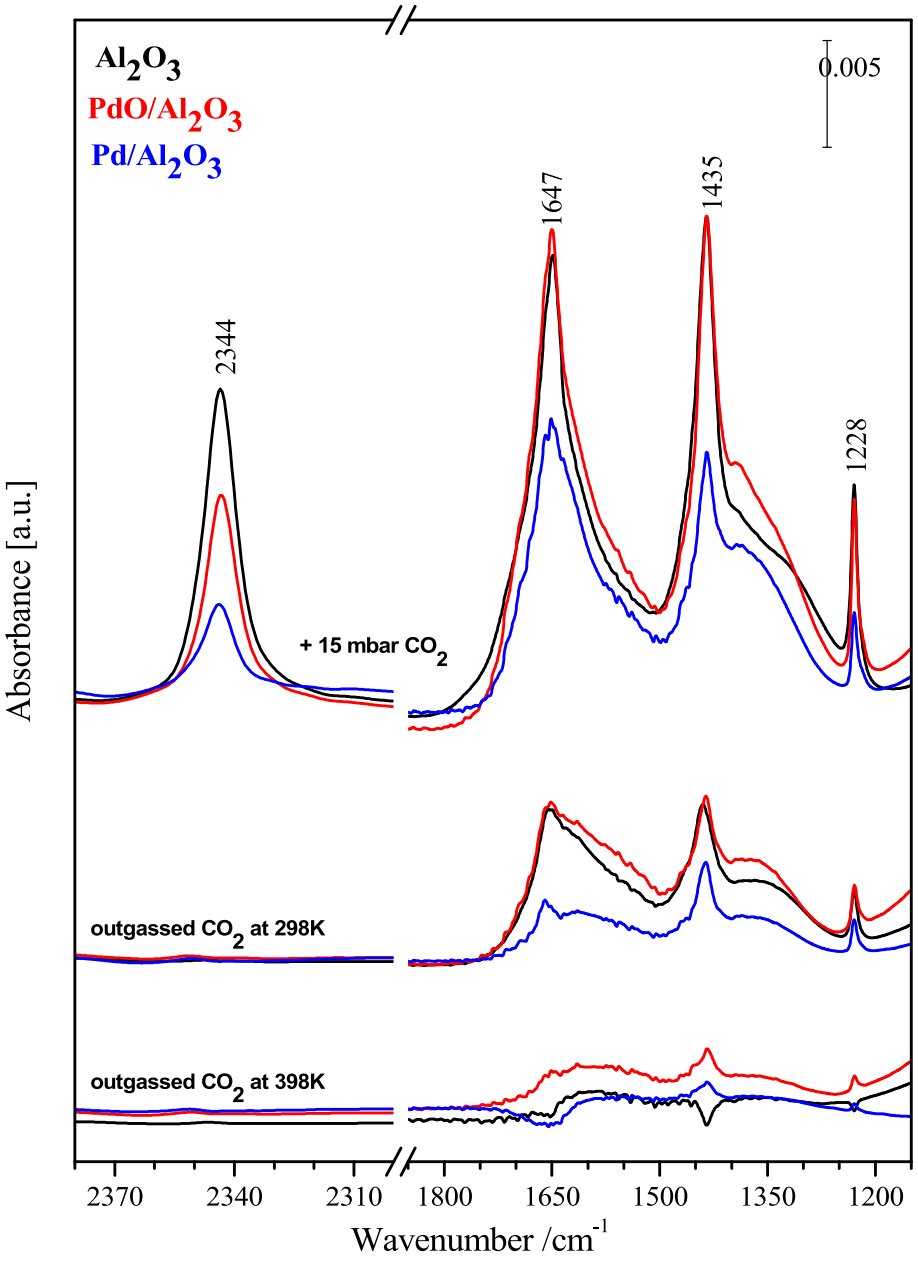

Fig. 9. FTIR difference and normalized spectra of Al_2O_3 (black curve), PdO/Al_2O_3 (red curve) and Pd/Al_2O_3 (blue curve) upon adsorption of CO_2 (15 mbar) at 25 °C (upper spectra), and after outgassing CO_2 at 25 °C (middle spectra) and 100 °C (lower spectra).

further band centered at 318 °C that can be attributed to medium-strong basic sites. By integrating the CO_2-TPD profiles, the density of the latter band is 195 μmol.g^{-1}. The CO_2-TPD profile was also measured on PdO/Al_2O_3 (Fig. 13B, Table S2 entry 2). The profiles are similar to that of fresh Al_2O_3, but the bands centered at 87, 125 and 195 °C are not observed, which is consistent with partial dehydroxylation of alumina during Pd impregnation. In contrast, an additional band appears that is centered at 253 °C. The band belonging to medium-strength acid sites is also visible at 325 °C with a density of basic sites of 177 μmol.g^{-1}.

5. Conclusion

γ-Alumina spheres calcined at 400 °C revealed as a robust and scalable acid catalyst for the aldol condensation/crotonization reaction of furfural and methyl isobutyl ketone (MIBK) in the temperature range of 120–180 °C. The catalyst reached full conversion of furfural into (E)-1-(furan-2-yl)-5-methylhex-1-en-3-one with almost complete carbon balance in batch mode at 160 °C for 12 h. The crotonization reaction was enhanced for a furfural conversion higher than 20 %. The reaction rate decreased at higher furfural concentration, which can be explained by the inhibition of Lewis acid centers due to adsorbed FF as inferred from kinetic modeling. The apparent activation energy is about 38 kJ/mol, which is much lower than the value measured on microporous and hierarchical H-SAPO-5 catalysts (~100 kJ/mol), suggesting a higher activation of FF on Lewis acid compared to Brønsted acid centers. The spent catalyst could be restored and reused for at least six consecutive catalytic runs without apparent loss of activity due to a lack of poisoning of active Lewis acid centers of medium strength during the reaction as inferred by FT-IR spectroscopy implemented with adsorbed pyridine and NH_3-TPD.

By impregnating alumina spheres with palladium, we conceived a single-reactor tandem process for the aldol condensation/crotonization reaction between furfural and methyl isobutyl ketone (MIBK), followed by hydrogenation with molecular H_2, to access tetrahydrofuran and

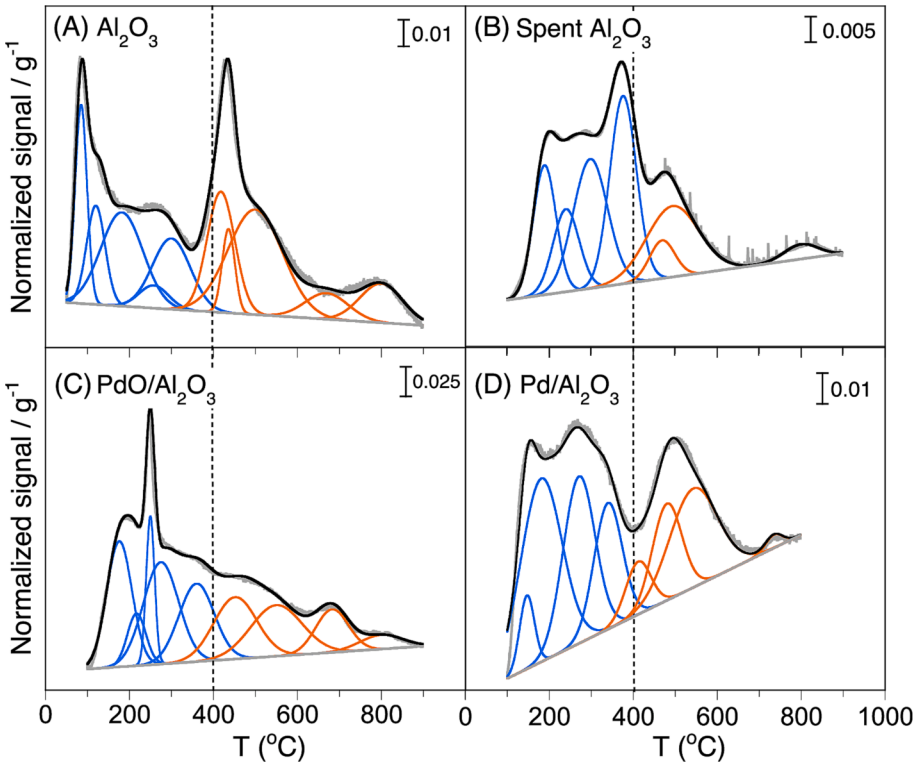

Fig. 10. NH_3-TPD profiles of (A) Al_2O_3, (B) spent Al_2O_3, (C) PdO/Al_2O_3 and (D) Pd/Al_2O_3 (crushed spheres, powder grinded at 200 μm). The peak deconvolution can be found in the SI (Table S1). The dash line indicates the calcination temperature (400 °C). The blue and orange deconvolution bands refer to acid sites below and upper the calcination temperature, respectively.

furan derivatives. The catalyst reached an overall 86 % yield of 1-(tetrahydrofuran-2-yl)-5-methylhexan-3-one in batch mode at 180 °C for 9 h for 5.2 wt% furfural concentration. The catalyst could also be operated at high furfural concentration (18 wt%) in a dual-type continuous fixed bed reactor reaching 55 % furfural conversion and 60 % and 35 % selectivity to 1-(furan-2-yl)-5-methylhexan-3-one and (E)-1-(furan-2-yl)-5-methylhex-1-en-3-one, respectively, after 12 h continuous operation at 170 °C and a WHSV of 0.50 h^{-1}.

This study opens up an avenue for engineering continuous flow reactors for tandem reactions based on furfural at high concentration to promote its stability under operation, making them compatible for industrial applications.

Declaration of Competing Interest

The authors declare that they have no known competing financial interests or personal relationships that could have appeared to influence the work reported in this paper.

Data availability

No data was used for the research described in the article.

Acknowledgements

This project has received funding from the European Union's Horizon 2020 research and innovation program under grant agreement N. 720783-MULTI2HYCAT.

Appendix A. Supplementary material

Quantification of mass transfer resistance on the catalyst; validation of plug flow regime in dual fixed-bed reactor; kinetic plots over Siral 5 HPV in Taiatsu and Top Industrie reactors; scheme of the setup used for catalytic tests in dual fixed-bed reactor; time-evolution of the carbon balance in the aldol condensation/crotonization reaction; time-evolution and parity plots for fitted and experimental TON; parity plots for fitted and experimental weight concentrations; comparison of catalytic performance of Al_2O_3 and Pd/Al_2O_3 spheres in the aldol condensation/crotonization reaction; catalytic performance of Al_2O_3 spheres in fixed-bed reactor for the aldol condensation/crotonization reaction; catalytic performance of Pd/Al_2O_3 spheres in single-reactor fixed-bed reactor for the aldol condensation/crotonization reaction – hydrogenation process; PXRD patterns of Al_2O_3 and PdO/Al_2O_3; representative HR-TEM micrograph of crushed Pd/Al_2O_3 spheres and size distribution of Pd nanoparticles; FTIR spectra of Al_2O_3, PdO/Al_2O_3 and Pd/Al_2O_3 spheres; CO_2-TPD profiles of Al_2O_3 and PdO/Al_2O_3 crushed spheres. Supplementary data to this article can be found online at https://doi.org/10.1016/j.cej.2023.145021.

References

[1] G.W. Huber, S. Iborra, S. Corma, Chem. Rev. 106 (2006) 4044–4098.
[2] A. Koutinas, C. Du, R.H. Wang, C. Webb, Introduction to Chemicals from Biomass, Wiley, Hoboken, 2008, p. 77.
[3] D.M. Alonso, J.Q. Bond, J.A. Dumesic, Green Chem. 12 (2010) 1493–1513.
[4] M. Dusselier, M. Mascal, B.F. Sels, B.F. Top, Curr. Chem. 353 (2014) 1–40.
[5] J.N. Chheda, J.A. Dumesic, Catal. Today 123 (2007) 59–70.
[6] R.J. van Putten, J.C. van der Waal, E. de Jong, C.B. Rasrendra, H.J. Heeres, J.G. de Vries, Chem. Rev. 113 (2013) 1499–1597.
[7] R. Mariscal, P. Maireles-Torres, M. Ojeda, I. Sádaba, M. López Granados, Energy Environ. Sci. 9 (2016) 1144–1189.
[8] J. Thoen, R. Busch, Industrial Chemicals from Biomass – Industrial Concepts, in: B. Kamm, P.R. Gruber, M. Kamm (Eds.), Biorefineries-Industrial Processes and Products: Status Quo and Future Directions, Wiley, 2005, pp. 347–365, chapter 12.
[9] G.W. Huber, J.N. Chheda, C.J. Barrett, J.A. Dumesic, Science 308 (2005) 1446–1450.
[10] J.P. Lange, J.-P. van der Heide, J. van Buijtenen, R. Price, ChemSusChem. 5 (2012) 150–166.
[11] J.Q. Bond, A.A. Upadhye, H. Olcay, G.A. Tompsett, J. Jae, R. Xing, D.M. Alonso, D. Wang, T. Zhang, R. Kumar, A. Foster, S.M. Sen, C.T. Maravelias, R. Malina, S.R.

H. Barrett, R. Lobo, C.E. Wyman, J.A. Dumesic, G.W. Huber, Energy Environ. Sci. 7 (2014) 1500–1523.
[12] M.J. Climent, A. Corma, S. Iborra, Green Chem. 16 (2014) 516–547.
[13] X. Li, P. Jia, T. Wang, ACS Catal. 6 (2016) 7621–7640.
[14] A. Patil, S. Shinde, S. Kamble, C.V. Rode, Energy & Fuels 33 (2019) 7466–7472.
[15] J.M. Rubio-Caballero, S. Saravanamurugan, P. Maireles-Torres, A. Riisager, Catal. Today 234 (2014) 233–236.
[16] A. Gumidyala, B. Wang, S. Crossley, Sci. Adv. 2 (2016) e1601072.
[17] M. Shirotori, S. Nishimura, K. Ebitani, Catal. Sci. Technol. 4 (2014) 971–978.
[18] J. Zhang, Y. Liu, S. Yang, J. Wei, L. He, L. Peng, X. Tang, Y. Ni, A.C.S. Sust, Chem. Eng. 8 (2020) 5584–5594.
[19] T. Komanoya, T. Kinemura, Y. Kita, K. Kamata, M. Hara, J. Am. Chem. Soc. 139 (2017) 11493–11499.
[20] D. Chandra, Y. Inoue, M. Sasase, M. Kitano, A. Bhaumik, K. Kamata, H. Hosono, M. Hara, Chem. Sci. 9 (2018) 5949–5956.
[21] C.P. Jiménez-Gómez, J.A. Cecilia, C. García-Sancho, R. Moreno-Tost, P. Maireles-Torres, ACS Sust. Chem. Eng. 7 (2019) 7676–7685.
[22] Y. Lou, S. Marinkovic, B. Estrine, W. Qiang, G. Enderlin, ACS Omega 5 (2020) 2561–2568.
[23] N. Alonso-Fagúndez, M.L. Granados, R. Mariscal, M. Ojeda, ChemSusChem. 5 (2012) 1984–1990.
[24] S. Monticelli, L. Castoldi, I. Murgia, R. Senatore, E. Mazzeo, J. Wackerlig, E. Urban, T. Langer, V. Pace, Monatshefte für Chemie 148 (2017) 37–48.
[25] D.O. Lolya, K.K. Venter, E.E. Liepin'sh, M.A. Trushule, S.A. Giller, Chem. Heterocyclic Compounds 12 (1976) 502–507.
[26] G. Li, N. Li, Z. Wang, C. Li, A. Wang, X. Wang, Y. Cong, T. Zhang, ChemSusChem. 5 (2012) 1958–1966.
[27] L. Bui, H. Luo, W.R. Gunther, Y. Roman-Leshkov, Angew. Chem. Int. Ed. 52 (2013) 8022–8025.
[28] X. Chen, L. Zhang, B. Zhang, X. Guo, X. Mu, Sci. Rep. 6 (2016) 28558.
[29] M. Douthwaite, X. Huang, S. Iqbal, P.J. Miedziak, G.L. Brett, S.A. Kondrat, J. K. Edwards, M. Sankar, D.W. Knight, D. Bethell, G.J. Hutchings, Catal, Sci. Technol. 7 (2017) 5284–5293.
[30] X.-L. He, H.-R. Zhao, C.-Q. Duan, X. Han, W. Du, Y.-C. Chen, Chem. Eur. J. 24 (2018) 6277–6281.
[31] C. Xu, E. Paone, D. Rodríguez-Padrón, R. Luque, F. Mauriello, Chem. Soc. Rev. 49 (2020) 4273–4306.
[32] R.M. West, Z.Y. Liu, M. Peter, C.A. Gaertner, J.A. Dumesic, J. Mol. Catal. A: Chem. 296 (2008) 18–27.
[33] H. Li, Z. Xu, P. Yan, Z.C. Zhang, Green Chem. 19 (2017) 1751–1756.
[34] W. Shen, G.A. Tompsett, K.D. Hammond, R. Xing, F. Dogan, C.P. Grey, W. Curtis Conner Jr., S.M. Auerbach, G.W. Huber, Appl. Catal. A: Gen. 392 (2011) 57–68.
[35] M. Sádaba, R. Ojeda, R. Mariscal, M. Richards, López Granados, Catal. Today 167 (2011) 77–83.
[36] M. Sádaba, R. Ojeda, J.L.G. Mariscal, M. Fierro, López Granados, Appl. Catal. B: Environ. 101 (2011) 638–648.
[37] L. Faba, E. Díaz, S. Ordónez, Appl. Catal. B: Environ. 113–114 (2012) 201–211.
[38] J. Cueto, L. Faba, E. Diaz, S. Ordonez, ChemCatChem. 9 (2017) 1765–1770.
[39] A. Bohre, M.I. Alam, K. Avasthi, F. Ruiz-Zepeda, B. Likozar, Appl. Catal. B: Environ. 276 (2020), 119069.
[40] L. Hora, V. Kelbichova, O. Kikhtyanin, O. Bortnovskiy, D. Kubicka, Catal. Today 223 (2014) 138–147.
[41] L. Hora, O. Kikhtyanin, L. Capek, O. Bortnovskiy, D. Kubicka, Catal. Today 241 (Part B) (2015) 221–230.
[42] O. Kikhtyanin, Z. Tisler, R. Velvarska, D. Kubicka, Appl. Catal. A: Gen. 536 (2017) 85–96.
[43] O. Kikhtyanin, S. Kadlec, R. Velvarska, D. Kubicka, ChemCatChem. 10 (2018) 1464–1475.
[44] F. Chen, N. Li, S. Li, J. Yang, F. Liu, W. Wang, A. Wang, Y. Cong, X. Wang, T. Zhang, Catal. Commun. 59 (2015) 229–232.
[45] L. Ao, W. Zhao, Y.-S. Guan, D.-K. Wang, K.-S. Liu, T.-T. Guo, X. Fan, X.-Y. Wei, RSC Adv. 9 (2019) 3661–3668.
[46] N.T. Dong, O. Kikhtyanin, R. Ramos, M. Kothari, P. Ulbrich, T. Munshi, D. Kubicka, Catal. Today 277 (2016) 97–107.
[47] G. Liang, A. Wang, X. Zhao, N. Lei, T. Zhang, Green Chem. 18 (2016) 3430–3438.
[48] A. Philippou, M.W. Anderson, J. Catal 189 (2000) 395–400.
[49] O. Kikhtyanin, R. Bulanek, K. Frohlich, J. Cejka, D. Kubicka, J. Mol. Catal. A: Gen. 424 (2016) 358–368.
[50] O. Kikhtyanin, Y. Ganjkhanlou, D. Kubicka, R. Bulanek, J. Cejka, Appl. Catal. Gen. 549 (2018) 8–18.
[51] W. Li, M. Su, T. Zhang, Q. Ma, W. Fan, Fuel 237 (2019) 1281–1290.
[52] O. Kikhtyanin, V. Kelbichova, D. Vitvarova, M. Kubu, D. Kubicka, Catal. Today 227 (2014) 154–162.
[53] O. Kikhtyanin, P. Chlubna, T. Jindrova, D. Kubicka, Dalton Trans. 43 (2014) 10628–10641.
[54] J. Cueto, V. Korobka, L. Faba, E. Diaz, S. Ordonez, A.C.S. Sust, Chem. Eng. 8 (2020) 4371–4383.
[55] M. Su, W. Li, Q. Ma, S. Li, T. Yang, X. Dou, Energy Fuels 33 (2019) 12518–12526.
[56] A. Al-Ani, C. Freitas, V. Zholobenko, Micropor. Mesopor. Mater. 293 (2020), 109805.
[57] Y. Jing, Y. Xin, Y. Guo, X. Liu, Y. Wang, Chin. J. Catal. 40 (2019) 1168–1177.
[58] E. Yuan, W. Dai, G. Wu, N. Guan, L. Li, Micropor. Mesopor. Mater. 305 (2020), 110361.
[59] M. Su, W. Li, T. Zhang, H. Xin, S. Li, W. Fan, L. Ma, Catal. Sci. Technol. 7 (2017) 3555–3561.
[60] G. Morales, M. Paniagua, D. de la Flor, M. Sanz, P. Leo, C. Lopez-Aguado, H. Hernando, S.A. Orr, K. Wilson, A.F. Lee, J.A. Melero, Fuel 339 (2023), 127465.
[61] C.J. Barrett, J.N. Chheda, G.W. Huber, J.A. Dumesic, Appl. Catal. B: Environ. 66 (2006) 111–118.
[62] W. Dedsuksophon, K. Faungnawakij, V. Champreda, N. Laosiripojana, Bioresource Technol. 102 (2011) 2040–2046.
[63] C. Ki, D. Ding, Q. Xia, Y. Wang, ChemSusChem. 9 (2016) 1712–1718.
[64] M. Gu, Q. Xia, X. Liu, Y. Guo, Y. Wang, ChemSusChem. 10 (2017) 4102–4108.
[65] L. Faba, E. Diaz, S. Ordonez, Catal. Today 164 (2011) 451–456.
[66] J. Yang, N. Li, G. Li, W. Wang, A. Wang, X. Wang, Y. Cong, T. Zhang, ChemSusChem 6 (2013) 1149–1152.
[67] M. Li, X. Xu, Y. Gong, Z. Wei, Z. Hou, H. Li, Y. Wang, Green Chem. 16 (2014) 4371–4377.
[68] L. Faba, E. Diaz, S. Ordonez, ChemSusChem. 7 (2014) 2816–2820.
[69] L. Gao, I. Miletto, C. Ivaldi, G. Paul, L. Marchese, S. Coluccia, F. Jiang, E. Gianotti, M. Pera-Titus, J. Catal. 397 (2021) 75–89.
[70] M.C. Hernandez-Soto, C. Segarra, F. Rey, U. Diaz, M. Pera-Titus, Appl. Catal. A: Gen. 643 (2022), 118710.
[71] H.J. Cho, D. Kim, J. Li, D. Su, B. Xu, J. Am. Chem. Soc. 140 (2018) 13514–13520.
[72] H.J. Cho, D. Kim, B. Xu, ACS Catal. 10 (2020) 4770–4779.
[73] S. Jiang, C. Ma, E. Muller, M. Pera-Titus, F. Jerôme, K. De Oliveira Vigier, ACS Catal. 10 (2019) 8893–8902.
[74] S. Jiang, E. Muller, M. Pera-Titus, F. Jerôme, K. De Oliveira Vigier, ChemSusChem. 13 (2020) 1699–1704.
[75] T. Barzetti, E. Selli, D. Moscotti, L. Forni, J. Chem. Soc., Faraday Trans. 92 (1996) 1401–1407.
[76] F. Jing, B. Katryniok, M. Araque, R. Wojcieszak, M. Capron, S. Paul, M. Daturi, J.-M. Clacens, F. De Campo, A. Liebens, F. Dumeignil, M. Pera-Titus, Catal. Sci. Technol. 6 (2016) 5830–5840.
[77] F. Jing, B. Katryniok, S. Paul, L. Fang, A. Liebens, B. Hu, F. Dumeignil, M. Pera-Titus, ChemCatChem. 9 (2017) 258–262.
[78] C. Morterra, G. Magnacca, Catal. Today 27 (1996) 497–532.
[79] X. Liu, R.E. Truitt, J. Am. Chem. Soc. 119 (1997) 9856–9860.
[80] A.A. Khaleel, K.J. Klabunde, Chem. Eur. J. 8 (2002) 3991–3998.
[81] C.A. Emeis, J. Catal. 141 (1993) 347–354.
[82] J. Shen, R.D. Cortright, Y. Chen, J.A. Dumesic, J. Phys. Chem. 98 (1994) 8067–8073.
[83] J. Szanyi, J.H. Kwak, Phys. Chem. Chem. Phys. 16 (2014) 15117–15125.
[84] J. Szanyi, J.H. Kwak, Phys. Chem. Chem. Phys. 16 (2014) 15126–15138.
[85] F. Solymosi, A. Berkò, J. Catal. 101 (1986) 458–472.
[86] F. Solymosi, J. Mol. Catal. 65 (1991) 337–358.
[87] H.-J. Freund, M.W. Roberts, Surf. Sci. Rep. 25 (1996) 225–273.